RESEARCH ARTICLE

Optical Beam Steering in FSO Systems Supported by Computer Vision

ANDRÉ C. CAMPOS[1], (Member, IEEE),
PETIA GEORGIEVA[2], (Senior Member, IEEE),
MARCO A. FERNANDES[1], (Member, IEEE),
PAULO P. MONTEIRO[1], (Senior Member, IEEE),
GIL M. FERNANDES[1], (Member, IEEE),
AND FERNANDO P. GUIOMAR[1], (Senior Member, IEEE)

[1]Instituto de Telecomunicações, Universidade de Aveiro, Aveiro 3810-193, Portugal
[2]Institute of Electronics and Informatics Engineering of Aveiro (IEETA), Campus Universitário de Santiago, Aveiro 3810-193, Portugal

Corresponding author: André C. Campos (andrecampos25@ua.pt)

ABSTRACT Free-Space Optical (FSO) communications have emerged as a viable solution to complement conventional communication technologies, mainly due to their high transmission rates, ease of implementation, low cost, and unlicensed spectrum. However, FSO technology faces significant challenges in achieving the initial alignment between the transceivers without pre-alignment or extensive manual configuration. The manual alignment process is extremely time-consuming and current automated solutions typically employ an infrared (IR) beam followed by an IR camera, which, besides increasing the transceiver cost, also requires an initial pre-convergence stage resorting to complementary coarse alignment technologies (e.g. Global Positioning System (GPS)). To tackle this challenge, we propose a novel methodology for the automatic alignment of FSO systems that does not require pre-convergence and avoids the use of costly IR cameras. The proposed alignment method is based on the application of computer vision (CV) during the transmission of a visible beacon and the utilization of pointing, acquisition and tracking (PAT) mechanisms. This solution is cost-effective, as the initial coarse alignment is carried out using visible light equipment, such as a standard CMOS camera and a visible beacon. Furthermore, it does not require any additional pre-convergence stage, since the alignment is based on characteristics acquired through CV during the transmission of the visible beacon, specifically the angle of inclination and the count of the number of pixels associated with the beacon. Additionally, the alignment process allows for a maximum angular misalignment of ± 3.3 degrees between the optical antennas (OA), corresponding to a coverage area of 5.3m^2 at a distance of 20 meters. Finally, using this method, the successful alignment of an FSO system is demonstrated in a free-space link with 20 meters distance for different ambient light conditions, with real-time transmission at 16 Gbps.

INDEX TERMS Free-space optics, pointing, acquisition and tracking mechanisms, automatic alignment, computer vision.

The associate editor coordinating the review of this manuscript and approving it for publication was Yogendra Kumar Prajapati.

I. INTRODUCTION

With the implementation of Fifth Generation (5G) technologies, the ongoing discussion on the Sixth Generation (6G)

and the increase in the number of devices requiring high bandwidths, the development of new high-capacity wireless communication technologies becomes crucial. Additionally, the congestion of the Radio-Frequency (RF) spectrum, coupled with the intrinsic limitations of this technology, requires alternatives. In this way, Free-Space Optical (FSO) communications are increasingly attracting the scientific community's interest, as they emerge as a viable solution to significantly improve the performance and reliability of wireless networks [1].

FSO provides a very wide bandwidth, when compared to RF links, allowing much higher data rates [2]. Concerning system implementations, FSO communications are much easier to install than typical fiber optics, requiring only a Line-of-Sight (LOS) connection between the transmitter and receiver. Additionally, FSO links do not require licensing, and operational costs are much lower [3]. Regarding security, FSO communications are challenging to intercept as this technology employs a highly directional beam in the infrared (IR) range with a very narrow beam divergence, which also prevents eavesdropping attacks. In addition, electromagnetic and radio frequency interference do not affect FSO communications, which is an issue in RF systems [4].

Based on the advantages of FSO systems, it is clear that this technology can be used in a variety of applications. Initially, FSO communications attracted attention by providing an efficient solution to the "last mile" problem [2]. This problem arises when a location is unsuitable for installing a fiber optic link or the excavation costs are too high [5]. In this way, FSO systems can be easily connected to fiber optic systems, bridging the gap between the end user and the transport network, thus enabling high-speed multi-campus connectivity [6]. More recently, FSO has become very attractive to be applied not only in the current generation (5G) but also for the next generation (6G) of mobile access [7]. In this context, a vertical expansion of the wireless network is also being prepared, namely resorting to Unmanned Aerial Vehicles (UAV), which have gained recent popularity due to their strategic positioning in the stratosphere [8]. This facilitates almost stationary and highly reliable LOS communication, mainly due to the absence of weather events in this region of operation [9]. Also fostered by the 3D network expansion that will be promoted by 6G, we are currently witnessing a rapidly growing interest in the exploitation of FSO systems to enhance the capacity of satellite communications [10], [11].

Despite the significant advantages and growing market that FSO systems present, this technology still faces challenges and limitations that affect its effective implementation. Terrestrial FSO systems use the atmosphere as a data transmission medium. Therefore, they are susceptible to adverse weather conditions that can compromise the quality of communication. Phenomena such as atmospheric turbulence and absorption can cause variations in optical signal propagation, resulting in significant losses and degradations

in the transmitted signal [4], [12]. In addition, precise alignment between transceivers is a critical challenge in all FSO systems, with an inaccurate alignment leading to pointing errors, suboptimal Angle of Arrival (AoA), and consequently substantial power losses at the receiver side [13]. To ensure correct alignment between transceivers, PAT mechanisms compensate for beam misalignments [14], [15]. Another highly challenging task in the implementation of FSO is the initial alignment between optical heads without prior knowledge. This initial setup, without pre-alignment or extensive manual configuration, is crucial in enabling optical communication [16]. Thus, PAT techniques play a critical role in satisfying LOS communication between a transmitter and a receiver and have emerged to combat or reduce possible pointing errors in FSO links, making systems more robust [13], [17]. In this way, PAT mechanisms have the function of aligning the transmitter with the receiver (pointing), ensuring that the optical signal is incident on the receiver (acquisition), and maintaining signal alignment throughout optical communications (tracking) [15]. The alignment process through PAT mechanisms is typically divided into coarse and fine. Starting from an FSO system where the transceivers do not have any prior characterization or information about the system and are misaligned, it is necessary to implement PAT mechanisms to perform coarse alignment of the system. Therefore, the primary role of coarse PAT is to achieve an initial alignment between the transmitter and receiver of the FSO system, allowing for a subsequent precise alignment of the system [18]. Commonly employed coarse PAT mechanisms are based on camera or Global Positioning System (GPS) technology [19], [20], [21]. It is important to note that the joint implementation of these mechanisms in an FSO system is possible, allowing for multi-stage coarse alignment mechanisms or for error correction in the event of failure of one of them. Subsequently, the fine PAT stage complements coarse PAT, aiming to achieve greater precision in the alignment between the transceivers of an FSO system. This stage aligns the transceivers to optimize optical communications through mechanisms that allow fine and precise adjustments. In this way, fine PAT can effectively correct minor disturbances that may arise during the transmission of information in the FSO system, such as pointing errors and fluctuations in the angle of arrival [22]. In this context, fine PAT mechanisms can be implemented using a multitude of devices such as gimbals, mirrors, and adaptive optics, assisted by tailored algorithms that aim to maximize the received optical power. Moreover, it is possible to create hybrid PAT solutions that integrate the advantages of each type of mechanism, potentially optimizing the precision of alignment and Field of View (FoV) between transceivers in FSO systems.

In this paper, we propose a robust technique capable of effectively performing the initial coarse alignment between transceivers in FSO systems, with the possibility of being combined with a more refined and precise second alignment

stage. To achieve this, we developed an automatic alignment method based on PAT mechanisms (camera and gimbal), a computer vision (CV) framework, and the transmission of a visible beacon. The use of a visible beacon for the initial coarse alignment allows to employ a simple CMOS camera to obtain its transmission characteristics, enabling the development of a more cost-effective solution compared to existing alignment methodologies that rely on IR cameras, for example, the mechanism presented in [19]. Furthermore, the use of a CMOS camera allows compatibility with CV techniques supported by a low-cost and low-power Raspberry Pi (RP) platform. This not only increases the energy efficiency and accessibility of the solution but also emerges as a novel approach compared to existing technologies. In terms of complexity, our method presents the advantage of enabling a standalone coarse PAT, avoiding the need for a pre-convergence coarse PAT using additional technology, such as in works [16], [19], and [21], which require the use of both GPS and cameras for coarse alignment. Thus, through the implementation of the proposed automatic alignment method, the obtained results demonstrate the effectiveness of the method in automatically aligning an FSO system in real-time, with a data transmission rate of 16 Gbps for a link length of 20 m.

The remainder of this paper is organized as follows. Section II describes the implementation of the proposed automatic alignment method, utilizing a visible light beacon assisted by CV for the initial alignment process. A detailed algorithm architecture is presented, responsible for fully aligning the system, as comprehensively demonstrated by a set of obtained experimental results. Section III details the experimental validation of the proposed CV-based method for performing the alignment of an FSO system over a distance of 20 m. Section IV describes the experimental validation of the proposed automatic alignment method with real-time optical communications at 16 Gbps. Finally, Section VI presents the main conclusions withdrawn from this work.

II. FSO ALIGNMENT ASSISTED BY COMPUTER VISION
A. IMPLEMENTATION CONCEPT
The proposed method for the automatic alignment of FSO systems utilizes an innovative technique, characterized by the transmission of two light beams with distinct wavelengths through an Optical Antenna (OA), a visible beacon (for coarse alignment), and an IR beam (for fine alignment and communications), as illustrated in Figure 1.

The alignment process is divided into two fundamental phases. In the first phase, the initial coarse alignment of the system is achieved using computer vision, utilizing information from the emission of the visible beacon to align the transmitting OA (OA_{TX}) with the CMOS camera. The application of the OpenCV framework to process the captured images, along with the compatibility of the CMOS camera with the control unit (RP), enables beam steering control, ensuring precise alignment between OA_{TX} and the camera. In the second phase, the aim is to perform a fine alignment
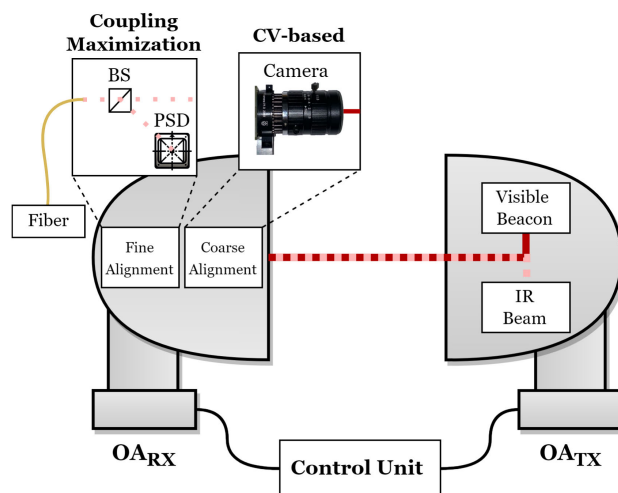

FIGURE 1. Conceptual illustration of the proposed FSO automatic alignment based on a visible beacon, computer vision, IR position sensing and power maximization.

based on optical power maximization, aligning OA_{TX} with the receiving OA (OA_{RX}). Starting from the aligned position between OA_{TX} and the CMOS camera, this phase only depends on the information acquired through the IR beam emission. For this purpose, OA_{RX} is assisted by a Beam Splitter (BS) and a Position-Sensing Detector (PSD). The IR beam is reflected by the BS and directly hits the PSD, allowing for the precise determination of the IR beam incident position on the PSD. Thus, based on this information, the orientation of OA_{TX} is adjusted, enabling the reception of optical power at OA_{RX} and ensuring a precise alignment of the FSO system.

1) COST-EFFECTIVE FSO ALIGNMENT USING A VISIBLE BEACON
In order to implement an algorithm capable of aligning the FSO receiver and transmitter units, images obtained by the RP camera from different orientations of the OA_{TX} were analyzed. Figure 2 illustrates the considered scenario, where a visible beacon is transmitted by the OA in front of the camera lens and the corresponding images are obtained by the RP camera at the receiver side. It is important to note that the photos of the visible beacon have been digitally zoomed in and captured with the lens aperture set to a value close to the maximum close-up, aiming to enhance the visibility of the beacon and eliminate possible noise caused by ambient light. In addition, the camera lens was focused on the plane of the OA. Analyzing the photos, as shown in Figure 2, it was observed that the beacon takes an elliptical shape when it is misaligned with the camera lens and a star shape when the beacon is close to the center of the camera lens.

By considering the different orientations of the OA with respect to the camera lens, it is possible to find an explanation for the shapes of the visible beacon in the photo captures. If the visible beacon is misaligned with the camera, the
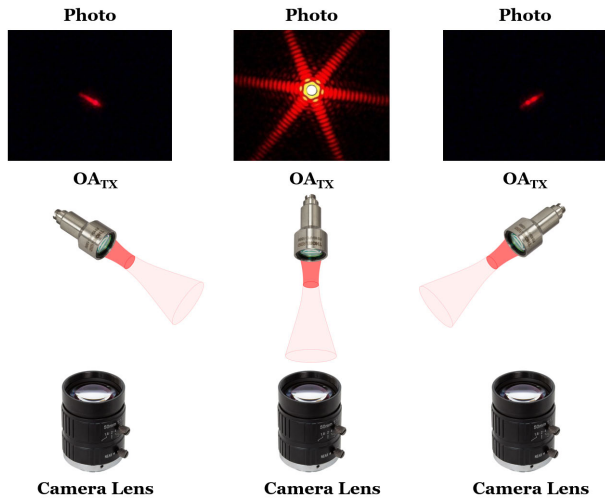
FIGURE 2. Characterization of the shape of the visible beacon for different OA orientation angles.

beam presents an elliptical shape in the captured photo. This phenomenon can be observed in Figure 2, where it can be seen that depending on the angle at which the visible beacon is observed, the ellipse depicted by the visible beacon changes according to its angle of inclination. This is because the beacon has a circular cross-section, and when observed at an angle other than frontal, the beam will appear as an ellipse. It is important to note that this phenomenon is not limited to the lateral misalignment of the beam since the same process occurs when the beacon is vertically misaligned.

On the other hand, the star shape shown in images captured when the beacon is aligned with the camera lens can be explained by combining three factors: camera sensor light saturation, light diffraction, and the geometry of the lens aperture. The saturation of pixels in the center of the six-pointed star can be explained by the extremely high central intensity of the beacon, which the camera sensor cannot capture, resulting in a saturation zone in the beacon image. Light diffraction occurs by light interference with itself, such as when it passes through an aperture or the edges of an obstacle. The size of the generated curvature depends on the relationship between the light wavelength and the size of the aperture, since apertures smaller than the wavelength produce greater diffraction [23], [24]. In addition, the diffraction of light is also influenced by the geometry of the aperture [25]. Finally, the diffraction pattern generated by a hexagonal aperture resembles the results obtained when the visible beacon hits the camera lens during the system characterization. Therefore, as the camera lens used in the experimental setup has a hexagonal aperture, the visible beacon in the captured images will have a six-pointed star shape.

2) OPENCV FRAMEWORK
In order to characterize the locations of the visible beacon when misaligned with the camera, we began by analyzing the characteristics of the observed ellipse through its angle

of orientation. Using the OpenCV library, detecting and describing objects with an elliptical shape in an image is possible. A Python script was developed to obtain the angle of inclination of the ellipse, and Figure 3 illustrates the execution of the computer vision steps detailed in Algorithm 1.
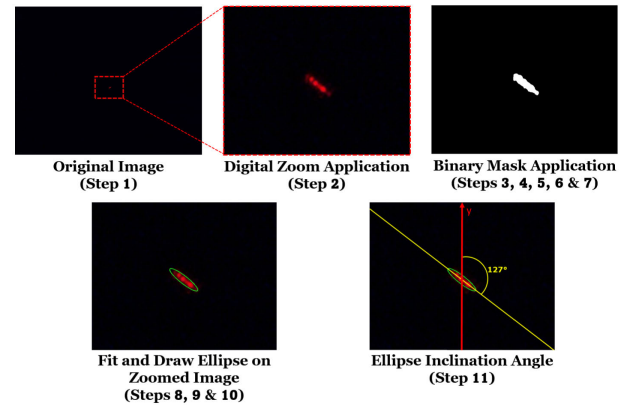

FIGURE 3. Computer vision steps for estimation of the ellipse inclination angle formed by the visible beacon.

Initially, a manual digital zoom was applied around the beacon, which made it easier and simpler to apply the methods presented later. Next, the contours in the image were detected. A Gaussian filter was applied to smooth the image and reduce noise. Subsequently, the image was converted to the HSV color space, commonly used in image processing, as it facilitates the definition of color ranges. Then, binary masks were applied to identify the red pixels in the image that fell within a specific range corresponding to the color of the beacon. In this process, red pixels within the band were defined as white, while pixels outside the band were defined as black. In addition, a morphological opening operation was performed on the binary mask using a specific kernel. This operation removes noise and details in the binary image through erosion followed by dilation, making it possible and easy to detect the contours [26], [27].

Based on the performed transformations, contours were identified in the resulting binary image, enabling the ellipse fit. Through the application of the ellipse fitting procedure, it was possible to obtain characteristics such as the position of the center of the ellipse, the lengths of the major and minor axes of the ellipse, and the angle of inclination of the ellipse. Thus, based on these characteristics, it was possible to represent the fitted ellipse accurately, as shown in Figure 3. The angle of inclination of the ellipse is defined as the angle between the ellipse's major axis and the image y-axis. The angles range from 0 to 180 degrees, in which the values 0 and 180 degrees indicate a vertical orientation of the ellipse, while 90 degrees indicate a horizontal orientation of the ellipse. Following, an example of a Python algorithm (see Algorithm 1) for obtaining the inclination angle of the ellipse formed by the transmission of the visible beacon is presented.

For more details, the entire developed code, along with image datasets, is available on GitHub [28].

Algorithm 1 Computer Vision Steps for Estimation of the Ellipse Inclination Angle

---

Input: Image captured from the visible beacon
Output: Ellipse Inclination Angle

1: **Load image:** `img = cv2.imread();`
2: **Apply manual digital zoom around the beacon**;
3: **Smooth image to reduce noise:**
   `smooth_img = cv2.GaussianBlur(img);`
4: **Convert image to HSV color space:**
   `hsv_img = cv2.cvtColor(smooth_img);`
5: **Define binary masks using color ranges:**
   `masks = cv2.inRange(hsv_img);`
6: **Combine binary masks:**
   `mask = cv2.bitwise_or(masks);`
7: **Apply morphological operations to binary masks:**
   `opening = cv2.morphologyEx(mask);`
8: **Find contours of visible beacon:**
   `contour = cv2.findContours(opening);`
9: **Fit ellipse to the found contours:**
   `ellipse = cv2.fitEllipse(contour);`
10: **Draw ellipse on zoomed image:**
   `cv2.ellipse(ellipse);`
11: **Ellipse inclination angle:**
   `inclination_angle = ellipse[2];`

In order to study the variation in the inclination angle of the ellipse, a wide range of azimuth and elevation orientations for the OA_{TX} has been scanned, generating a 2D matrix whose entries are associated with the position of the beacon projected at the receiver plane. For each one of these scanned positions, an image was captured and processed according to the above methodology to calculate the angle of inclination of the ellipse, as shown in Figure 4a. Based on the colormap shown in Figure 4, it can be concluded that there are well-defined regions where the ellipse tends to align itself with vertical (0 and 180 degrees) or horizontal (90 degrees) orientations when compared to the y-axis. Thus, based on the angle of inclination of the ellipse, it is possible to characterize all the positions resulting from the complete 2D sweep, except the zone highlighted in white in Figure 4. The presence of the white color indicates that an ellipse cannot be drawn in the respective captured images and, consequently, the corresponding inclination angles cannot be obtained. When analyzing this occurrence, it was found that in areas where the beacon is partially or completely aligned with the camera, it does not have the characteristic elliptical shape anymore.

To characterize the spatial region identified by the white color in Figure 4a, we studied the variations in the number of red pixels present in each image captured during the execution of the full 2D scan, using the `cv2.countNonZero()` function. To use this function, the binary images previously
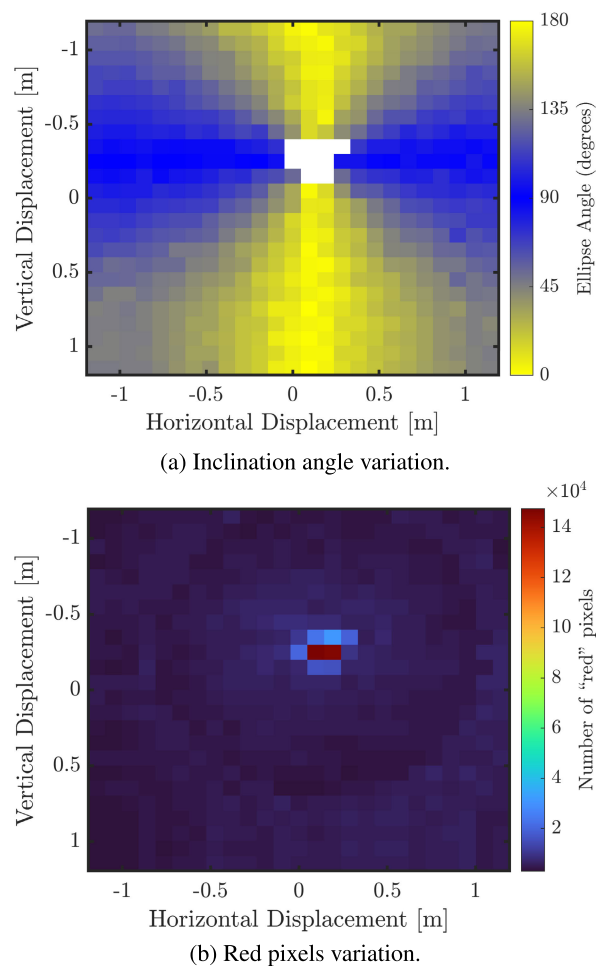

(a) Inclination angle variation.

(b) Red pixels variation.

FIGURE 4. Characterizing the inclination angle and the number of red pixels of the visible beacon for a full 2D sweep; a) ellipse inclination angle; b) number of red pixels.

obtained for contour detection were supplied as input arguments. In this way, the `cv2.countNonZero()` function returns the count of non-null pixels (white pixels) in each binary image, and the results of this count are shown in Figure 4b. It can be seen that the positions with the highest number of red pixels coincide with the positions where it is impossible to obtain the inclination angles of the ellipse, which correspond to the positions closest to the precise alignment between the beacon and the camera lens. Thus, a robust approach to unequivocally characterize the 2D position of the beam at the receiver plane can be achieved by jointly considering the information provided in Figures 4a and 4b, i.e. by utilizing both the detection of the ellipse's inclination angle (in a first stage) and the count of red pixels present in each image captured by the camera (in a second stage).

B. MULTI-STAGE ADAPTIVE BEAM ALIGNMENT ALGORITHM

In order to align an FSO system, the proposed alignment process is divided into two distinct phases: coarse and fine

alignment. First, a coarse alignment is performed to minimize the alignment error between the transmitter and receiver OAs. This coarse alignment is based on the information obtained by applying CV to the images captured by the camera lens and the characterization of a transmitted visible beacon, as presented in Subsection II-A. Subsequently, in the second alignment phase, a refined alignment is based on the power measurement of the IR beam. To achieve this, an alignment is performed based on information from a PSD, and finally, a Gradient Descent (GD) is performed to maximize the received optical power. Through this algorithm architecture, it will be possible to align the FSO system when the transceivers are initially misaligned and have no prior information about the system.

Figure 5 illustrates the complete architecture of the alignment algorithm, divided into two phases and four stages. The four stages will be presented in detail subsequently.

1) 1ST STAGE - INITIAL COARSE ALIGNMENT

The first stage aims to perform the initial coarse alignment so that the alignment error is within a few centimeters of the ideal aiming point. To this end, the information obtained from the visible beacon is used, such as the ellipse inclination angles and the red pixel count.

At this stage, the process begins without any prior information. Through the characterization of the ellipse angles and the red pixel count, numerous positions emerge that share the same characteristics when the beacon is not incident on the camera, which introduces difficulties in determining the initial position of the beacon. Therefore, the alignment process should start by acting on the OA_{TX} to sweep the beam position at the receiver plane either over the x or y axes. Without loss of generality, let us consider in this work that this initial sweep is then performed over the x-axis, i.e. over a horizontal line projected at the receiver plane. For each new position along the x-axis, the angle of inclination of the ellipse is stored in the array. The characterization of the ellipse inclination angles, presented in Figure 4a, shows that the beacon is vertically aligned with the camera when along the x-axis, the ellipse has a vertical orientation, i.e., an inclination angle of 0 or 180 degrees. Thus, after scanning all positions along the x-axis and comparing the stored ellipse inclination angles, the utilized PAT mechanism should move the beacon to the position corresponding to the optimal vertical orientation of the ellipse.

Next, starting from the position where the x-axis was aligned, the y-axis alignment starts. In this way, the same process is repeated as before, but this time, going through all positions on the y-axis, checking the red pixel count while the x-axis remains fixed. In this way, for each new position along the y-axis, the corresponding count of red pixels is stored, and at the end of the scan, the PAT should move the beacon to the position with the highest count of red pixels. Thus, the beacon must be close to or incident on the camera lens at the new position on the x and y axes.

2) 2ND STAGE - GRADIENT DESCENT BASED ON RED PIXELS COUNT

In order to ensure that the visible beacon is perfectly incident on the camera lens, a GD optimization based on red pixels count is performed. Implementing the GD algorithm aims to find the image with the maximum red pixel count, resulting in the visible beacon being accurately incident on the camera lens.

The GD is an iterative optimization algorithm used in general minimization problems. In this way, the algorithm moves toward the steepest gradient, iteratively calculating the next point using the gradient at the current position. In addition, it adjusts the step size based on a defined learning rate and subtracts the value obtained from the current position, moving step by step in the direction to minimize the cost function [29]. In this case, the GD algorithm had to be adapted to the goal of finding the position with the highest red pixel count, as detailed in Figure 6.

Starting from time instant $k = 1$, stage 2 begins with finding the next position along the x-axis, $x(k + 1)$. This is done by counting the number of red pixels, $N(1)$, at the starting position of the algorithm $[x(1), y(1)]$. Since the maximum number of red pixels is unknown a priori, a dynamic target had to be inserted into the GD algorithm. Thereby, the GD maximization target is adaptively defined by adding ΔN to the initially measured number of red pixels, i.e. $N_{\max}(k) = N(k) + \Delta N$. In this way, the next position on the x-axis, $x(k + 1)$, is obtained using the following expression:

$$x(k + 1) = x(k) + f(N(k), N_{\max}(k)), \qquad (1)$$

where $f(\cdot)$ defines the GD cost function. Next, after moving to the new position on the x-axis $[x(k + 1), y(k)]$, a similar process is applied over the y-axis,

$$y(k + 1) = y(k) + f(N(k), N_{\max}(k)). \qquad (2)$$

After moving to the new x- or y-axis positions, the count of the number of red pixels, $N(k)$, is updated and compared with the current target value, $N_{\max}(k)$. If $N(k)$ reaches the value of $N_{\max}(k)$, the value of $N_{\max}(k)$ is updated by incrementing ΔN, which was empirically set to $\Delta N = 7 \times 10^4$ in the specific scenario of this work. Otherwise, j alignment attempts are made up to a maximum limit of $j_{\max} = 5$ to achieve the goal. However, if the goal is not reached after $j_{\max}$ iterations, it is concluded that the algorithm has entered in a saturation zone. This means that the latest value set for $N_{\max}(k)$ already exceeds the maximum value of red pixels that can be achieved in the system, and consequently, it is ensured that the visible beacon is perfectly aligned with the camera. The cost function, $f(\cdot)$, used in the expressions (1) and (2) is defined as,

$$f(N(k), N_{\max}(k)) = \mu \operatorname{sign}(N(k) - N(k - 1))$$
$$\times |N_{\max}(k) - N(k)|, \qquad (3)$$

where μ represents the learning rate, $\operatorname{sign}(N(k) - N(k - 1))$ indicates the optimization direction and $|N_{\max}(k) - N(k)|$
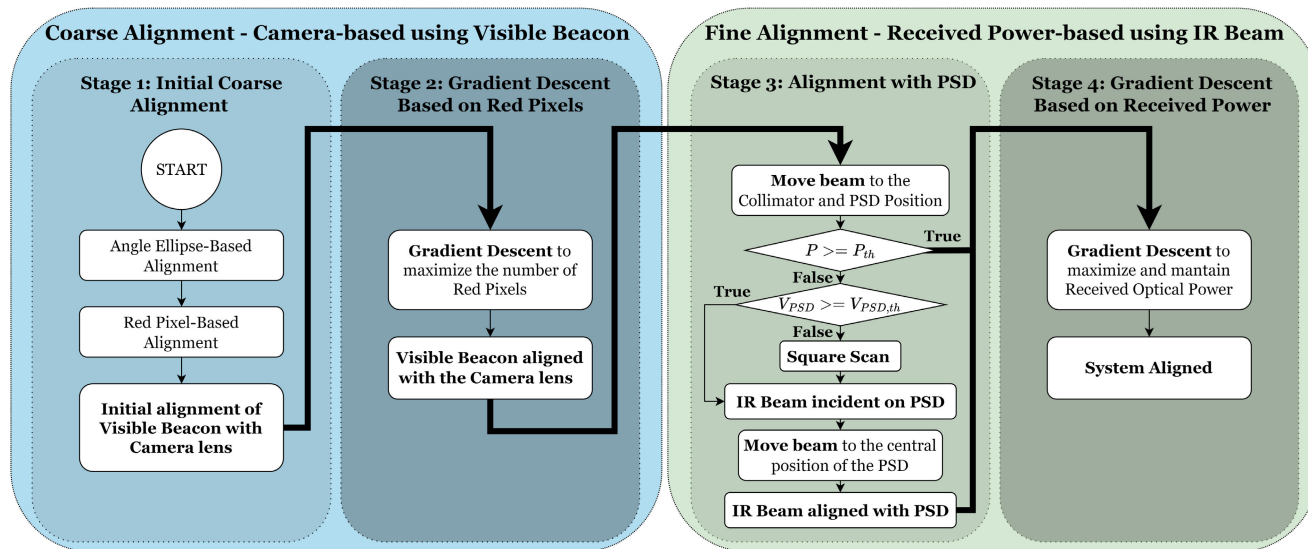
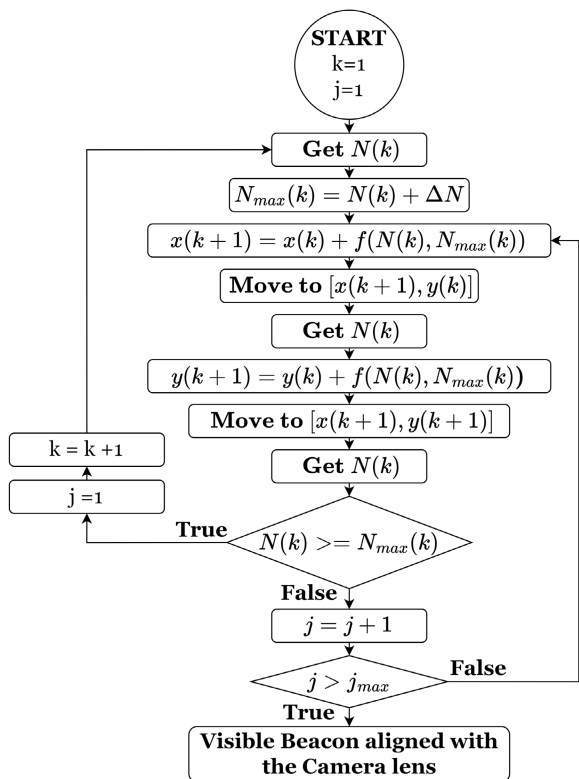**FIGURE 5.** Proposed system alignment algorithm architecture.

FIGURE 6. GD-based algorithm to maximize the number of red pixels during the 2nd stage optical beam alignment of Figure 5.

become highly time-consuming if the learning rate is too low. It is, therefore, essential to find the right balance when setting the learning rate. In this work, a learning rate of $\mu = 5 \times 10^{-4}$ has been found to provide a good fit to the problem at hands.

The direction of movement is determined by the function $\text{sign}(N(k) - N(k-1))$, where the function $\text{sign}(\chi)$ is defined as,

$$\text{sign}(\chi) = \begin{cases} 1, \chi \geq 0 \\ -1, \chi < 0. \end{cases} \quad (4)$$

The input argument of this function is the difference between the current value of the red pixel count and the value of the previous position, i.e., $N(k) - N(k-1)$. If this value is greater than zero, the function's maximum is in that direction. Otherwise, it indicates that the PAT direction needs to be reversed since the function's maximum is in the opposite direction.

Finally, using $|N_{\max}(k) - N(k)|$, the error between the current red pixel count and the target to be reached is calculated, allowing the adaptive displacement at each step. Calculating the error plays a crucial role in the cost function, as it allows the PAT steps to be adaptively adjusted based on the magnitude of the error. When the errors are smaller, the PAT steps are smaller, and more precise. On the other hand, for large errors, the PAT steps are increased, facilitating faster convergence toward the defined red pixel count target.

With the completion of this stage, the visible light beacon is accurately aligned with the camera lens. In this way, the visible beacon can now be switched off and the following stages will be carried out based on the information-bearing IR beam, making it possible to receive the transmitted optical power.

quantifies the absolute error. The learning rate, μ, must be carefully chosen since it plays a crucial role in the determination of the step size and, consequently, the GD convergence. If the learning rate is too high, the desired maximum may be exceeded, and the system may start to diverge completely. However, the convergence process can

3) 3RD STAGE - ALIGNMENT WITH PSD

At this stage, a check is made to determine whether the beam is hitting the OA lens. To do this, the current received optical power, P, is compared with a given threshold power, P_{th}. If the current optical power is equal to or greater than the defined threshold power, the IR beam is aligned with the OA lens, allowing progression to stage 4. However, if the current power does not reach the required threshold power, this suggests that the beam is in a region close to the center of the OA lens, but not striking it correctly. In this case, a second check is carried out to determine whether the IR beam is incident on the PSD. For this second check, the total voltage obtained from the PSD, V_{PSD}, is assessed. If this is equal to or greater than a predefined minimum voltage limit that ensures optimal operation of the PSD, i.e., $V_{PSD} \geq V_{PSD,th}$, the algorithm assumes that the IR beam is indeed incident into the PSD. Otherwise, some error has affected the previous alignment, resulting in the beam being very close to the PSD but not striking it. In that case, a small square sweep is made around the position where the beam was left after the downward movement to solve this problem. The scan aims to find a position where the voltage sum present in the PSD, V_{PSD}, is equal to or greater than the predefined minimum voltage, $V_{PSD,th}$. When this condition is satisfied, it can be concluded that the beam is hitting directly on PSD.

Before applying the adjustment method that moves the beam to the center of the PSD, a prior calibration is conducted. This calibration is necessary because there is a BS in front of the OA_{RX}, which reflects a portion of the beam toward the PSD. The calibration ensures that when the IR beam hits the center of the PSD, the power received at the OA lens is greater than or equal to the target power. Therefore, to apply the adjustment method that moves the beam to the center of the PSD, the minimum voltage present in the PSD must be equal to or greater than $V_{PSD,th}$. Once this condition has been achieved, the IR beam is aligned with the center of the PSD. This configuration enables the comparison of the current position of the IR beam, $[x_{PSD}, y_{PSD}]$, with the central position of the PSD, which is defined as $[0, 0]$. In this way, the IR beam is precisely aligned with the center of the PSD using this comparison, resulting in a collimated optical power that should be above the threshold required to advance to the final alignment stage, as described in the following.

4) 4TH STAGE - GRADIENT DESCENT BASED ON RECEIVED POWER

The last stage of fine alignment is based on the direct monitoring of the optical power that is collimated into the receiving fiber. The objective is to align the IR beam with the OA lens to receive and maintain maximum power. Using the information from the received optical power, a GD approach is again performed, as detailed in Figure 7.

The GD method is based on the approach detailed in [30], where the optical power is continuously measured to keep the FSO link aligned. Its working principle is similar to
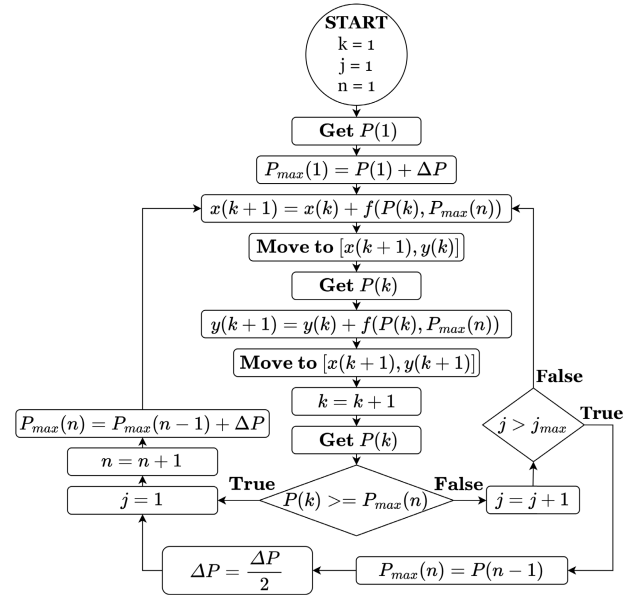

FIGURE 7. GD-based algorithm to maximize the received optical power during the 4th stage optical beam alignment of Figure 5.

the one described in stage 2, Subsection II-B2, changing only the objective function to maximize the received optical power instead of the red pixel count. The x and y positions during this beam alignment stage are then updated as follows,

$$x(k + 1) = x(k) + f(P(k), P_{\max}(n)),$$
$$y(k + 1) = y(k) + f(P(k), P_{\max}(n)), \quad (5)$$

where $P(k)$ is the measured received optical power at time instant k, and $P_{\max}(n)$ is the defined target of maximum received optical power. It is important to note that the received power is measured again between the update of the x and y positions, as shown in Figure 7. Following the same approach as for expression (3), the cost function for the power-based GD optimization is then defined as,

$$f(P(k), P_{\max}(n)) = \mu \, \text{sign}(P(k) - P(k - 1))$$
$$\times |P_{\max}(n) - P(k)|. \quad (6)$$

Note that, similarly to the optimization of the number of red pixels in the 2nd alignment stage, also the target of maximum received optical power is unknown a priori. Its value might depend on multiple system parameters, such as transmitted optical power, link distance and insertion loss at the OA. Therefore, akin to stage 2, we have chosen to implement a dynamic maximization target for the power optimization using the GD algorithm. To that end, a gradual power increment, ΔP, is defined. Taking into account the specific implementation scenario of this work, $\Delta P = 0.5 \, \text{dB}$ has been empirically defined, together with a maximum number of iterations $j_{\max} = 5$. Since this is the last alignment stage, where finer precision is required, a modification is introduced to the adaptive GD target, where the power increment is halved, $\Delta P = \Delta P/2$, whenever $j_{\max}$ is achieved, i.e. when

the algorithm enters its saturation zone. By doing so, the power target is finely adapted to the actual maximum optical power supported by the FSO system, thereby avoiding an oscillatory behavior when reaching a steady-state. Finally, for this power-based optimization, the learning rate value was set to $\mu = 0.035$, as it was verified after various tests that this value was the most suitable to guarantee the convergence of the system.

III. EXPERIMENTAL VALIDATION OF CV ASSISTED MULTI-STAGE ALIGNMENT

A. EXPERIMENTAL SETUP

To experimentally validate the proposed CV-assisted optical beam alignment technique described in the previous section, we have implemented the experimental setup depicted in Figure 8.

The transmitter PAT apparatus comprises two stepper motor actuators (Thorlabs ZST206) controlled by an RP 4B with 8GB RAM. According to the detailed specifications from the datasheet of the high-precision stepper motor actuators, these components have a 6 mm screw and support a maximum resolution of incremental screw displacement of 0.5 nm in high-precision mode, or 1 μm in standard operation mode. This implies that the stepper motors allow the use of microsteps, enabling the division of each step into 2048 substeps. The stepper motors were mounted on a compatible collimator holder (Thorlabs KM100) to allow adjustment of the fiber collimator orientation. This holder has two holes where the stepper motors will be inserted, and each of these holes is designed to accept a screw with a density of 80 threads per inch, corresponding to a displacement of 317.5 μm per thread. Therefore, through the maximum resolution of the stepper motors, it is possible to move approximately $1.6 \times 10^{-4}\% \left(\frac{0.5 \text{ nm}}{317.5 \ \mu m} \times 100 \right)$ of the total displacement of a single thread. Additionally, according to the datasheet, each thread corresponds to an angular resolution of 8 mrad. Thus, through the implementation of the stepper motors, it is possible to obtain a maximum angular resolution (θ) of the gimbal of approximately 13 nrad $\left(8 \text{ mrad} \times 1.6 \times 10^{-4}\% \right)$. Using this resolution, we calculated the maximum supported link distance (d) to achieve a minimum alignment precision (Δx) of, for example, 0.1 mm, obtaining $d \approx 8$ km given by $d = \frac{\Delta x}{\tan(\theta)}$. This precise control allows for the adjustment of the orientation of a fiber collimator (col1), which emits a visible beacon with a power of -9 dBm and a wavelength of 632 nm, as well as an IR beam with a power of 8 dBm and a wavelength of 1550 nm. It is important to note that the utilized fiber collimator (Thorlabs F810APC-1550) was designed to transmit beams with a wavelength of approximately 1550 nm. Therefore, the transmission of the visible beacon through this fiber collimator does not satisfy the specifications described in the datasheet, resulting in significant divergence. In addition, the fiber collimators used have a Field of View (FoV) of ± 3.3 degrees, enabling coverage of approximately 5.3 m^2 at a link length of 20 meters through the utilization of stepper motors.

On the receiver side, an RP High Quality (HQ) Camera equipped with a 50 mm lens is connected to the RP via a flex cable. The camera features a Sony IMX477R stacked sensor with a resolution of 12.3 megapixels. Below the camera lens, the FSO receiver includes a BS (Thorlabs BP208) followed by a fiber receiver collimator. The BS reflects 8% of the beam to a Ø2'' CaF2 Plano-Convex Lens (PCL) (Thorlabs LA5210), thus reducing the beam diameter to focus on the Quadrant Detector (QD) (Thorlabs PDQ30C). The QD is connected to the RP to provide information about the incidence positions of the IR beam on the photodiode sensor, which features an InGaAs substrate and a diameter of 3.0 mm. It is important to note that the QD only operates correctly when the total voltage exceeds the minimum defined threshold, which in this case is 0.2V. Finally, the fiber collimator (col2) is connected to a Power Meter (PM) to measure the received optical power. A picture of the experimental setup is shown in Figure 9, highlighting the transmitter and receiver PAT components.
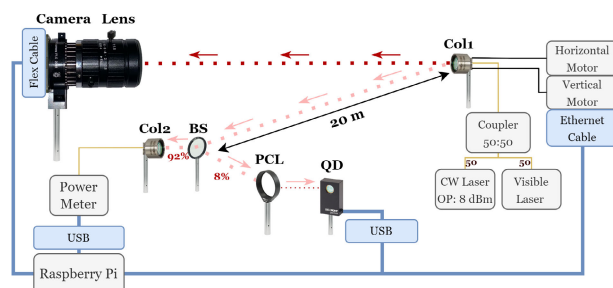

FIGURE 8. Experimental setup used for FSO automatic alignment. Symbol codes: ▪ ▪ ▪ visible beacon; ⋯ IR beam; ── optical fiber; ── connection cables.
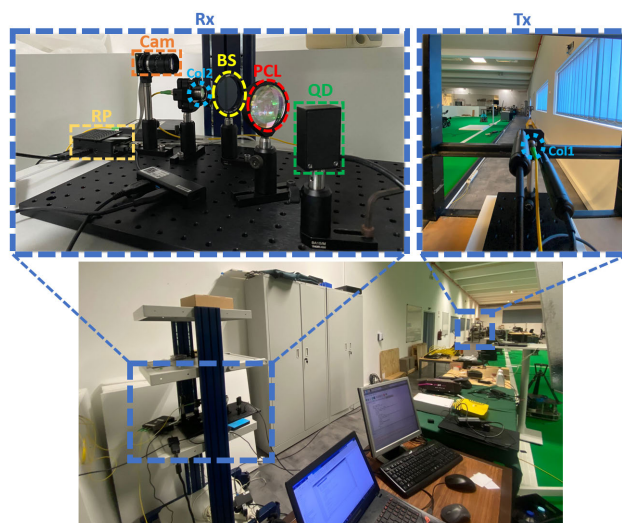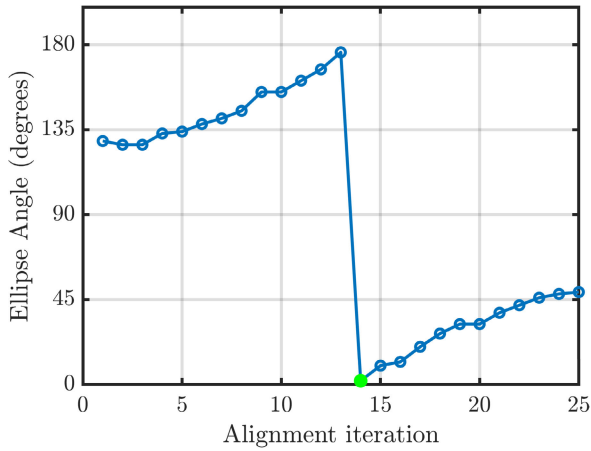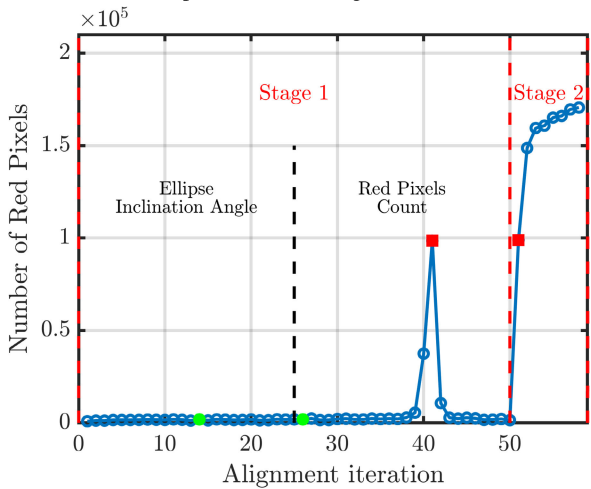

FIGURE 9. Picture of the experimental setup used for FSO automatic alignment.

B. EXPERIMENTAL RESULTS

Using the experimental setup presented in Figure 8 and 9, the architecture of the algorithm for the automatic alignment of FSO systems was implemented and experimentally validated.

(a) Ellipse inclination angle evolution.

(b) Red pixels evolution.

FIGURE 10. Evolution of the inclination angle and the number of red pixels during the alignment of the visible beacon with the camera lens for a link distance of 20 m; a) ellipse inclination angle; b) number of red pixels.

1) CV-BASED COARSE ALIGNMENT

Initially, through the implementation of stages 1 and 2, the aim is to align the visible beacon with the camera lens. Figure 10a shows the evolution of the ellipse inclination angle during an alignment attempt. As described in subsection II-B1, stage 1 starts with a process that sweeps all stepper motor positions along the x-axis to find the position corresponding to the orientation of the ellipse closest to the vertical formed by the transmission of the visible beacon, aligning the beacon vertically with the camera. This position of vertical alignment is identified in iteration 14, which is represented in Figure 10a by a green marker (◦). On the other hand, Figure 10 illustrates the evolution of the red pixel count. Since the beacon is initially completely misaligned with the camera, the red pixel count is nearly zero. The second process begins from the position where the beacon is vertically aligned with the camera, as indicated by a green point in Figure 10b. This process sweeps across the full y-axis range enabled by the utilized stepper motors, aiming to find the position corresponding to the highest red pixel count in

the captured images. Thus, the peak in the obtained results in stage 1 corresponds to the position of an initial coarse alignment between the beacon and the camera, represented in Figure 10b by a red marker (■). From this position, it was possible to implement the GD developed in stage 2 (described in detail in subsection II-B2) to maximize the red pixel count, resulting in a precise alignment between the visible beacon and the camera lens.

In order to test the robustness and consistency of successful alignments, 50 attempts were performed, as depicted in Figure 11.
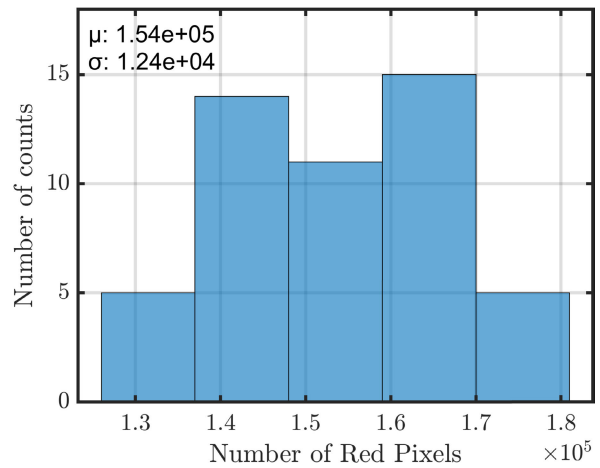

FIGURE 11. Histogram of visible beacon alignments with the camera lens for a link distance of 20 m.

Based on the obtained results, it can be concluded that stages 1 and 2 of the alignment algorithm succeeded since the beacon was aligned with the camera lens in all attempts, as the number of red pixels detected in each final captured image is high ($>10^5$) and falls within a well-defined region. As shown in Figure 4b in subsection II-A2, which represents the variation in the number of red pixels during the scan, it was found that the red pixel count is very close to zero when the beacon is not incident on the camera and reaches a maximum when the beacon is aligned with the camera. Thus, these results show that all alignment attempts have indeed been able to maximize the number of red pixels.

2) PSD-BASED FINE ALIGNMENT AND OPTICAL POWER MAXIMIZATION

Stage 3 of the alignment was then carried out. At this stage, the alignment process begins with the vertical downward movement of the col1 orientation by a predefined step size to direct the IR beam to the col2, installed below the camera lens, as depicted in Figure 8. Following this, as previously described in subsection II-B3, the objective of this stage is to obtain a sum of voltages in the QD greater than the defined minimum threshold of 0.2 V to ensure the device is able to work properly, and the results obtained from this stage are shown in Figure 12. This figure shows the 50 alignment attempts, together with the sum of the voltages associated

with each one. All attempts are above the minimum threshold, represented by the red line, which indicates that the beam alignment was 100% successful. In addition, Figure 12 also shows the attempts that did not require the square scan around the final position resulting only from the alignment of the visible beacon with the camera, represented by a red marker (·). This makes it possible to quantify the effectiveness of alignment with and without square scanning. Therefore, out of the 50 alignment attempts, 21 did not require square scanning, indicating that alignment based on the visible beacon alone yielded a moderated efficiency to focus the IR beam on the QD.
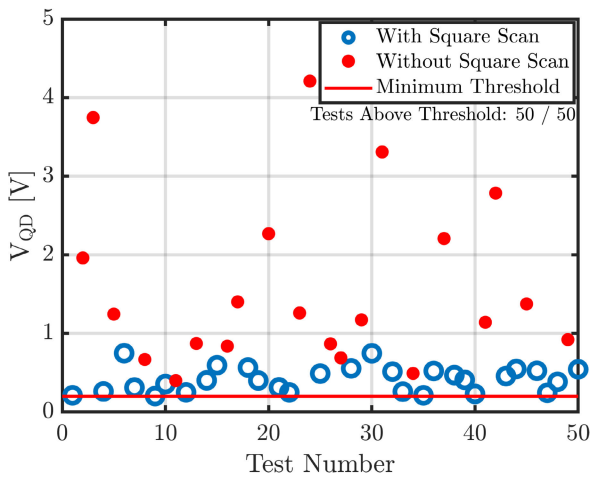

**FIGURE 12.** Alignment of the IR beam with the QD for a link distance of 20 m.

Once the IR beam is successfully aligned with the QD in all attempts, the final step of stage 3 is initiated, which involves the precise alignment of the IR beam with the central position of the QD. Given that the relative positions of the QD and receiver collimator have been previously calibrated, whenever the IR beam is centered on the QD, a significant portion of the optical beam should already be collimated into the optical fiber, thus allowing for a mensurable optical power to arrive at the monitoring optical power meter. The results of this process are depicted in Figure 13 in blue. It can be seen that in all alignment attempts, it was possible to obtain a received optical power above -1.1 dBm, which confirms the success of the alignment for a link distance of 20 m. Note that, in the system under test, the registered values of received optical power after the QD-based stage 3 alignment are already highly satisfactory, owing to the accurate calibration of the placement of the QD and receiver collimator devices. Nevertheless, for a more robust alignment process, a final power-based alignment stage should be considered, as described in the 4th stage of our proposed beam steering algorithm. This will help to circumvent any (mis)calibration issues associated with the positioning of the QD and receiver collimators (e.g. due to thermal stress or vibration), thus enabling to fine tune the optical beam alignment accuracy by directly maximizing

the collimated optical power, which is actually the ultimate target for the PAT subsystem. As previously described in subsection II-B4, this stage includes the application of a GD method based on the received optical power, and the results are represented in Figure 13 in red.

Thus, by comparing the results before (in blue) and after (in red) stage 4, it is evident that the introduction of stage 4 has a positive impact, stabilizing the received optical power. The received optical power values were effectively maximized, as they are close to the maximum value shown in blue in Figure 13a, and, on average, the 50 tests resulted in a received power of approximately -0.65 dBm. Furthermore, there was a reduction in the variation of the powers resulting from each alignment, with a standard deviation (σ) of approximately 0.03 dB, proving the accuracy of the alignment algorithm, as shown in Figure 13b.
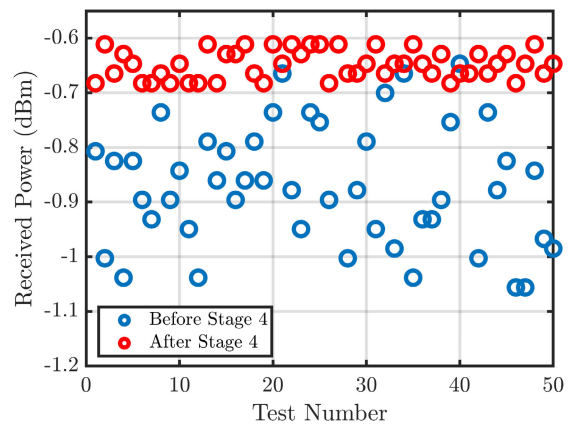
(a) Variations in received optical power before and after Stage 4.
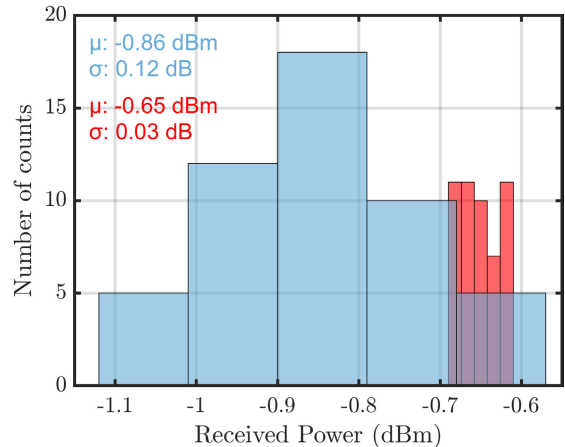
(b) Histogram of variations in received optical power before and after Stage 4.

FIGURE 13. Comparison of received optical power before and after the implementation of alignment Stage 4 at 20 m.

3) PERFORMANCE ASSESSMENT

Finally, three consecutive alignment tests were conducted to assess the behavior of the received optical power over time and to prove the precise alignment of an FSO system with a link distance of 20 m, as shown in Figure 14a.

By executing the stages outlined in the alignment algorithm detailed in Section II-B, the system is successfully aligned until it reaches a received optical power of around −0.65 dBm, with a transmission power of 8 dBm. Figure 14a shows that each alignment cycle takes approximately 5 minutes to reach a stable optical power over time, highlighting the speed of the alignment process, as it is the time it takes from deployment to the fully-functional operation of the FSO system. This stability can be clearly observed in the zoomed-in inset of the final part of the first alignment test, as shown in Figure 14b. In this figure, the received optical power remains constant at around −0.65 dBm for 4 minutes, which is also confirmed for the remaining alignment tests.
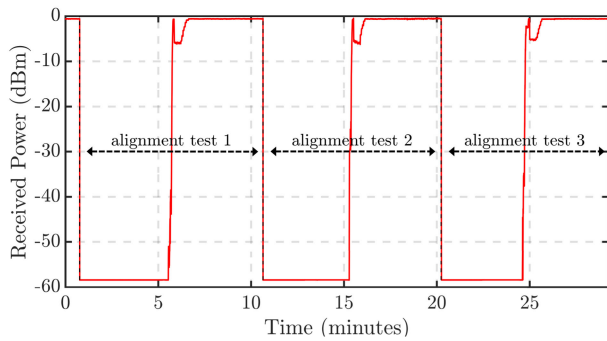
(a) Evolution of the received optical power during each alignment test.
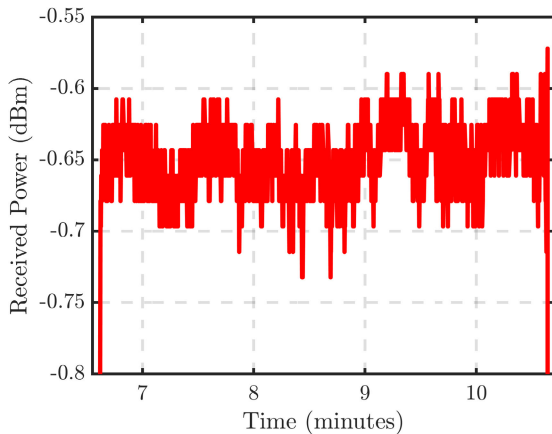
(b) Zoomed-in on the stability of received optical power in the first alignment test.

FIGURE 14. Behavior of received optical power during alignment tests at 20 m.

The ability to maintain a stable received optical power over time is achieved by implementing stage 4 of the alignment algorithm, which compensates for small disturbances that can occur on the FSO link. The initial power loss observed before stabilization is due to the behavior of the cost function used in the GD process of stage 4. This cost function determines the direction in which the stepper motors must move the beam to reach the position with the maximum received optical power. When the power received at the current position is compared to the power received at the previous position, and the previous power is higher, the alignment system adjusts the

beam's movement direction in response to the power drop. In this way, the system reacts immediately to the incurred power drop, maximizing and maintaining the received optical power over time.

IV. EXPERIMENTAL VALIDATION WITH REAL-TIME FSO TRANSMISSION

After validating the successful and stable acquisition of optical power in the previous section, it is now relevant to assess the FSO communication performance over the aligned link, in order to guarantee that the developed system is indeed compatible with high-speed transmission.

A. EXPERIMENTAL SETUP

To conduct optical communications over the implemented FSO system, the experimental setup illustrated in Figure 15 was developed. This experimental setup is similar to the one shown in Figure 8, although with modifications to the IR beam transmission and reception configuration. These changes were implemented because the previous setup only used a CW LASER to transmit an IR beam with a specific power. In this updated configuration, a Bit Error Rate Tester (BERT, Keysight Technologies - J-BERT M8020A) device was introduced, whose function is to quantify the Bit Error Rate (BER) present in the FSO system. This device generates a known test bit stream, transmits it over the communication channel, and then compares the resulting bit stream with the original one. The changes between the data streams are checked through direct bitwise comparison, and if there are any changes, they are recorded as bit errors. Collecting this information makes it possible to evaluate the FSO system performance in real-time.
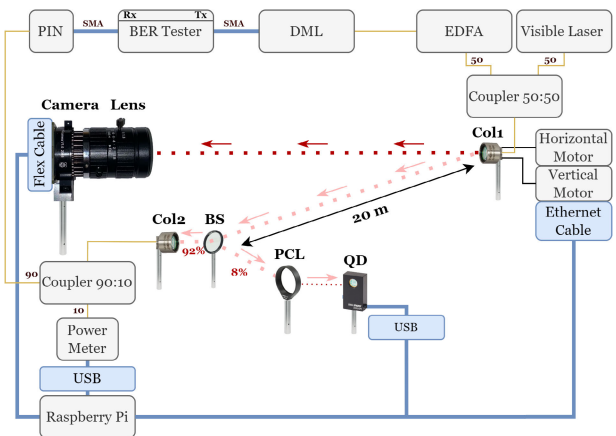
FIGURE 15. Experimental setup used for automatic beam alignment together with real-time optical communications over 20 m. Symbol codes: ▪ ▪ ▪ visible beacon; ⋯ IR beam; ▬▬ optical fiber; ▬▬ connection cables.

In this way, the signal transmission process was carried out at 16 Gbps data rate, generated by the BERT configured with Non-Return-to-Zero (NRZ) line coding. The signal was then transmitted via an SMA cable to modulate a Direct

Modulated Laser (DML, Oclaro TTA - 10 Gbps Tunable Transmitter C-band), generating a modulated IR light beam containing the test bits to be transmitted in the system. The modulated signal was subsequently amplified by an Erbium-Doped Fiber Amplifier (EDFA, Exelite Innovations - XLT-CFA Series) and combined with the visible beacon using a 50:50 coupler, enabling simultaneous transmission of the modulated IR beam and the visible beacon via col1. The components used for the alignment process and treatment of the received power were previously shown in Figure 8. However, a 90:10 coupler was added to the receiver side, allowing the BER to be quantified using the IR beam received at col2. Additionally, a PIN (Nortel Networks Optical Components - 10 Gb/s Preamp Receiver) was incorporated to convert the received optical signal into an electrical signal, which is routed to the BERT.
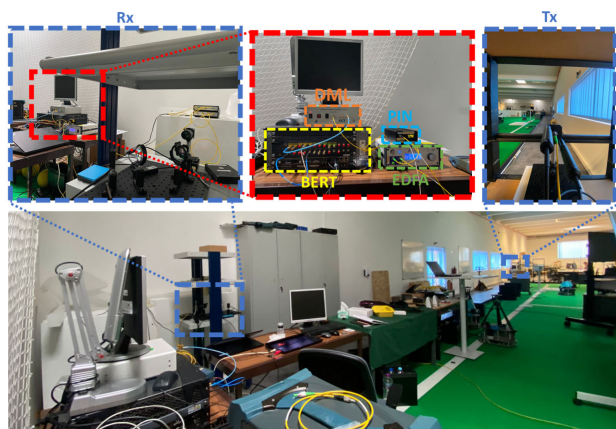

FIGURE 16. Picture of the experimental setup used for real-time optical communications over 20 m.

B. EXPERIMENTAL RESULTS

In order to experimentally validate the alignment method and conduct real-time optical communications, the automatic alignment described in Subsection II-B was carried out. By implementing the developed automatic alignment, it was possible to maximize the received optical power and evaluate the associated variations in BER, as shown in Figure 17.

When analyzing the obtained results, it is clear that the consecutive alignment attempts were successful. This observation is possible due to the well-defined zones in the graph, where the system went from a misaligned state, characterized by the absence of received optical power, to an aligned state after the execution of the implemented algorithm, resulting in a received optical power of roughly 0 dBm. At the same time, while the received optical power was being captured, the BER was calculated using the BERT. Analyzing Figure 17, it can be seen that the zones with the highest BER values coincide with the minimum power values, confirming the situation of total system misalignment. On the other hand, it can also be observed that the highest values of received optical power over time, delimited by dashed vertical lines, correspond to error-free transmission.

This demonstrates the successful alignment of the FSO system over a distance of 20 m, enabling real-time optical communications at 16 Gbps.

Although not shown in the paper for brevity, alignment tests were also carried out under different ambient lighting conditions. The developed CV-based method exhibited high robustness, since it took practically the same amount of time (approximately 5 minutes) to maximize and maintain a constant received optical power regardless of the ambient light conditions, thus indicating that the proposed methodology can be reliably applied to a wide range of indoor and outdoor FSO applications.
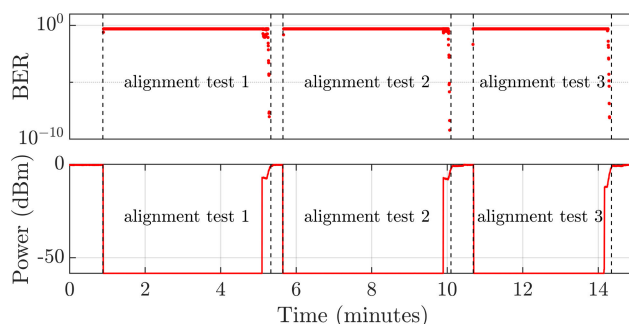

FIGURE 17. Variation of BER and received optical power over three successive alignment tests.

V. POTENTIAL APPLICATIONS AND CHALLENGES

After presenting and analyzing the proposed automatic alignment method, from the implementation concept to the obtained results, it becomes crucial to address the main challenges, mitigation strategies, and potential opportunities associated with its practical implementation.

Considering that the automatic alignment method has been successfully validated for a link distance of 20 meters in an indoor environment, its practical deployment may face different challenges depending on the targeted application scenario, as will be discussed in the following.

A. ENVISIONED APPLICATION SCENARIOS

For the purpose of accuracy/robustness assessment and initial prototyping of our newly proposed CV-based automatic alignment mechanism, in the course of this work, we have considered a stable indoor environment for validation purposes. Although this simplified assumption ignores the impact of critical channel impairments that are characteristic of outdoor weather-exposed environments, the obtained results are expected to find a good match with a set of indoor application scenarios such as intra-datacenter connectivity [31] and industry 5.0 [32]. Nonetheless, the developed multi-stage alignment methodology can also be adapted to operate in more challenging outdoor scenarios, such as inter-building communications [33], 6G fronthaul/backhaul [34], [35], last-mile access [36] and 3D optical wireless communications [37]. On that regard, a particularly promising approach involves the use of Unmanned Aerial Vehicle

(UAV) platforms complemented with FSO communications, as they offer easy deployment, cellular connectivity mainly due to the installation of base station entities, strong LOS links, controllable mobility, and services during emergencies or natural disasters [37], [38]. Consequently, the opportunity arises to implement the proposed alignment method on low-altitude platforms, such as free-flying UAVs.

B. PRACTICAL IMPLEMENTATION CHALLENGES
Despite their indisputable practical relevance, these other terrestrial application use cases pose new challenges to the automatic alignment subsystem, namely in terms of the impact of atmospheric turbulence and potential mechanical vibrations of the FSO optical heads, which should be properly addressed in order to extend the applicability of the proposed CV-based optical beam alignment methodology.

1) CHALLENGES TO THE COARSE ALIGNMENT SUBSYSTEM
Regarding the initial camera-based coarse alignment, the influence of atmospheric turbulence and/or vibrations on transceiver platforms can result in pointing errors, affecting the alignment accuracy between the visible beacon and the camera lens. This is expected to be particularly challenging for UAV-assisted FSO systems, which might be strongly impacted by both turbulence-induced beam wandering and propeller-induced vibrations. Nevertheless, as presented in subsection II-B2, the alignment algorithm includes a stage based on a GD method with an adaptive target to maximize the number of red pixels, allowing for more flexible and accurate coarse alignment even in challenging environments. This feature is crucial for adjusting the collimator orientation and compensating for fluctuations in beacon incidence positions caused by possible vibrations in the transceiver platform, ensuring consistent and stable coarse alignment. Nevertheless, to compensate for more intense vibrations on the transceiver platform, a viable solution would be to use a camera with more robust sensors and high-quality camera lens capable of capturing detailed information at higher frequencies. This would not only help compensate for potential errors in the incidence position of the visible beacon but also allow for increased FSO link distances, enabling better resolution of visible beacon transmission characteristics and more accurate coarse alignment. Finally, complementing this approach with advanced image processing techniques, possibly resorting to artificial intelligence (AI) techniques, might be crucial to ensure precise alignment in random and challenging conditions.

2) CHALLENGES TO THE FINE ALIGNMENT SUBSYSTEM
Regarding the fine alignment subsystem, which is based on the maximization of the fiber coupling efficiency of the IR beam, it is crucial to ensure extremely precise alignment to enable optical power reception. Such a precise alignment can be significantly affected by the combined effects of turbulence and other mechanical vibrations. Therefore, two complementary solutions should be considered:

- **avoid the interference of turbulence on pointing error mitigation:**
  Similarly to coarse alignment, in the refined alignment process, a GD method with an adaptive target is employed to maximize received optical power (detailed in subsection II-B4), thereby inherently providing the alignment method with the flexibility to support turbulence levels higher than those experienced in the tested indoor environment. On that regard, a critical point that should be carefully optimized depending on the characteristics of the turbulent channel is the optical power acquisition subsystem. Namely, sufficiently long power averaging should be considered in order to distinguish the impact of scintillation from the impact of actual pointing errors. However, this must be done without compromising the bandwidth of pointing error tracking itself. To alleviate this constraint, one should consider that the third step of the proposed alignment method presented in subsection II-B3 already utilizes a position sensor device. By continuously tracking the position of the incident IR beam on the PSD, it should be possible to isolate the impact of pointing errors from the impact of turbulence-induced scintillation. Therefore, in a highly turbulent FSO system the final 4th-stage power-based alignment subsystem should be redesigned to also receive frequent position coordinate updates from the 3rd-stage PSD-based subsystem.
- **perform active turbulence compensation:**
  Besides avoiding the interference of turbulence on the compensation of pointing errors, in strong turbulence regimes the PAT mechanism should also be able to incorporate some level of turbulence mitigation. To that end, it is also essential to consider that, to combat high levels of atmospheric turbulence, the speed and resolution of the alignment mechanism might be a limiting factor. Therefore, ensuring the stability of the PAT mechanism and potentially replacing the stepper motors used in the experimental setup with high bandwidth fine-tracking systems, such as fast-steering mirrors, may be crucial. Finally, another solution to compensate for the challenges of atmospheric turbulence is the integration of wavefront sensors and deformable mirror modules, which can complement the turbulence mitigation capabilities of the PAT system by dynamically correcting distortions and aberrations on the beam wavefront.

3) EXTENDING LINK DISTANCE
The proposed CV-based mechanism has demonstrated successful automatic alignments for a link length of 20 meters. However, addressing the challenges and finding solutions to extend the linking distance is crucial.

The coarse alignment of the system is achieved by transmitting a visible beacon using a fiber collimator designed for wavelengths in the IR range, resulting in a significant divergence of the visible beacon as the FSO link distance increases,

negatively impacting the precision of the initial alignment. One potential solution is to use two separate fiber collimators, one specifically for transmitting the visible beacon and another for the IR beam. However, this approach would increase the cost of the transceivers and the complexity of the alignment process, requiring meticulous synchronization and calibration of the fiber collimators. Additionally, as the link distance increases, cameras with high-resolution sensors and longer focal length lenses are required to capture the visible beacon's characteristics accurately. This requirement leads to increased costs and potential imposition of space and weight constraints on the transceivers. However, implementing the proposed solutions is expected to increase the link length to ranges between 50-100 meters, which may find applications in short-range FSO communications, such as dense inter-building connections, inter-rack links in datacenter networks, and industrial ambient connections.

To extend the supported link distances to medium- and long-range applications, potentially reaching linking distances on the order of kilometers, it may be necessary to switch from visible components to the use of IR beams and IR cameras. This approach enables the transmission of higher powers, as IR beams are safer for the human eye compared to visible beacons, which are essential for extensive FSO links. Furthermore, using IR cameras to capture the characteristics of the IR beam ensures more precise alignment, even in conditions of low visibility, as they are less affected by interference from ambient light sources. On this regard, an important future research direction involves the study of the geometrical properties of the misaligned optical beam when using an IR beacon. In particular, it is crucial to understand if the ellipticity features identified in subsection II-A1 can also be exploited when using an IR beacon, which would avoid the need for additional pre-alignment PAT stages (e.g. using GPS), as it is typically done nowadays when using IR beacons and cameras.

Therefore, depending on the target link length for implementation in the specific application scenario, it becomes crucial to evaluate the performance of automatic alignment using the most adequate optical elements (e.g. collimator lenses and camera objectives), as well as beacons with different wavelengths (e.g., visible and IR) and transmitted powers to find the most efficient solution (trade-off between performance, cost, eye safety, and power consumption).

4) SIZE, WEIGHT AND POWER CONSTRAINTS

In application scenarios where energy consumption and footprint are critical, as it is the case of UAV-FSO relay systems, the PAT subsystem might have to be re-designed in light of the imposed SWaP constraints. Considering that UAVs have limited flight time due to their battery capacity, it is crucial to carefully select the maximum allowable payload weight, potentially privileging the use of miniaturized fast-steering mirrors in detriment of a bulkier gimbal-based ATP. Additionally, energy management strategies should be implemented to optimize battery usage and extend the UAV's flight time. Therefore, the energy consumption associated with the processes of image acquisition, CV processing and active beam steering must be thoroughly inspected and minimized. In particular, the trade-off between the power expended for transmitting the visible beacon and the power required to detect the beacon shape through CV algorithms should be carefully optimized.

VI. CONCLUSION

The quickly expanding deployment of 5G systems and the fast advancement of novel 6G technologies have propelled FSO systems to become increasingly reliable to complement conventional communications technologies, mainly due to their high transmission rates, ease and low-cost implementation, and unlicensed spectrum. However, FSO technology faces critical challenges in achieving initial alignment between the transceivers without pre-alignment, extensive manual configuration, or prior system knowledge. In this work, we have proposed a CV-based method for performing the initial alignment of an FSO system using PAT mechanisms and the characteristics of a visible beacon's transmission. Firstly, the system was characterized to analyze the visible beacon's behavior for different pointing positions relative to the camera lens. This study led to the key observation that the visible beacon detected by the camera is characterized by an elliptical shape with different inclination angles when no portion of the beacon's footprint is directly incident on the camera lens. In turn, as the beacon approaches the position of alignment with the camera lens, it triggers a noticeable increase in the count of red pixels in the captured image. Thus, combining these characteristics obtained by CV with refined alignment algorithms using PAT mechanisms made it possible to develop an automatic alignment algorithm for FSO systems. Alignment tests were conducted at a link length of 20 m, and it was found that the system aligned automatically in all attempts, demonstrating the robustness of the proposed methodology, with each alignment attempt taking approximately 5 minutes. Additionally, it was verified that the OAs have a FoV of approximately ±3.3 degrees. This FoV corresponds to a coverage area of 5.3 m^2 at a distance of 20 m, ensuring that the alignment process can be successfully conducted, provided that both OAs are located within this coverage area. Finally, real-time optical communications were successfully demonstrated, with transmission rates of 16 Gbps achieving error-free operation after the automatic alignment is concluded. In summary, the developed solution offers significant advantages in terms of cost-effectiveness and the use of Commercial Off-The-Shelf (COTS) components (RP, CMOS camera), highlighting the economic affordability and implementation accessibility of this innovative methodology for automatic FSO system alignment.

REFERENCES

[1] S. Chen, Y.-C. Liang, S. Sun, S. Kang, W. Cheng, and M. Peng, "Vision, requirements, and technology trend of 6G: How to tackle the challenges of system coverage, capacity, user data-rate and movement speed," *IEEE Wireless Commun.*, vol. 27, no. 2, pp. 218–228, Apr. 2020.

[2] M. A. Khalighi and M. Uysal, "Survey on free space optical communication: A communication theory perspective," *IEEE Commun. Surveys Tuts.*, vol. 16, no. 4, pp. 2231–2258, 4th Quart., 2014.

[3] K. Anbarasi, C. Hemanth, and R. G. Sangeetha, "A review on channel models in free space optical communication systems," *Opt. Laser Technol.*, vol. 97, pp. 161–171, Dec. 2017.

[4] H. Kaushal and G. Kaddoum, "Optical communication in space: Challenges and mitigation techniques," *IEEE Commun. Surveys Tuts.*, vol. 19, no. 1, pp. 57–96, 1st Quart., 2017.

[5] A. Malik and P. Singh, "Free space optics: Current applications and future challenges," *Int. J. Opt.*, vol. 2015, pp. 1–7, Apr. 2015.

[6] H. A. Willebrand and B. S. Ghuman, "Fiber optics without fiber," *IEEE Spectr.*, vol. 38, no. 8, pp. 40–45, Aug. 2001.

[7] M. A. Fernandes, P. P. Monteiro, and F. P. Guiomar, "Free-space terabit optical interconnects," *J. Lightw. Technol.*, vol. 40, no. 5, pp. 1519–1526, Mar. 8, 2022.

[8] S. C. Arum, D. Grace, and P. D. Mitchell, "A review of wireless communication using high-altitude platforms for extended coverage and capacity," *Comput. Commun.*, vol. 157, pp. 232–256, May 2020.

[9] R. Samy, H.-C. Yang, T. Rakia, and M.-S. Alouini, "Space-Air-Ground FSO networks for high-throughput satellite communications," *IEEE Commun. Mag.*, vol. 61, no. 3, pp. 82–87, Mar. 2023.

[10] M. J. M. d. Freitas, "Fast and reliable beam steering technologies for free-space optics systems," M.S. thesis, Departamento de Electrónica, Telecomunicações e Informática (DETI), Universidade de Aveiro, Aveiro, Portugal, 2022.

[11] P. K. Sahoo and A. K. Yadav, "A comprehensive road map of modern communication through free-space optics," *J. Opt. Commun.*, vol. 44, no. 1, pp. s1497–s1513, Feb. 2024.

[12] O. Bouchet, H. Sizun, C. Boisrobert, and F. D. Fornel, *Free-Space Optics: Propagation and Communication*, vol. 91. Hoboken, NJ, USA: Wiley, 2010.

[13] M. A. Fernandes, B. T. Brandão, P. Georgieva, P. P. Monteiro, and F. P. Guiomar, "Adaptive optical beam alignment and link protection switching for 5G-over-FSO," *Opt. Exp.*, vol. 29, no. 13, pp. 20136, 2021.

[14] B. Skuse. (2023). *Free-space Optics To Connect the World*. [Online]. Available: https://spie.org/news/free-space-optics-to-connect-the-world?SSO=1

[15] Y. Kaymak, R. Rojas-Cessa, J. Feng, N. Ansari, M. Zhou, and T. Zhang, "A survey on acquisition, tracking, and pointing mechanisms for mobile free-space optical communications," *IEEE Commun. Surveys Tuts.*, vol. 20, no. 2, pp. 1104–1123, 2nd Quart., 2018.

[16] M. M. Abadi, M. A. Cox, R. E. Alsaigh, S. Viola, A. Forbes, and M. P. J. Lavery, "A space division multiplexed free-space-optical communication system that can auto-locate and fully self align with a remote transceiver," *Sci. Rep.*, vol. 9, no. 1, p. 19687, Dec. 2019.

[17] R. Abdelfatah, N. Alshaer, and T. Ismail, "A review on pointing, acquisition, and tracking approaches in UAV-based fso communication systems," *Opt. Quantum Electron.*, vol. 54, no. 9, p. 571, Sep. 2022.

[18] T.-H. Ho, *Pointing, Acquisition, and Tracking Systems for Free-Space Optical Communication Links*. College Park, ML, USA: University of Maryland, 2007.

[19] A. Carrasco-Casado, R. Vergaz, J. M. Sánchez-Pena, E. Otón, M. A. Geday, and J. M. Otén, "Low-impact air-to-ground free-space optical communication system design and first results," in *Proc. Int. Conf. Space Opt. Syst. Appl. (ICSOS)*, May 2011, pp. 109–112.

[20] K. Kazaura, K. Omae, T. Suzuki, M. Matsumoto, E. Mutafungwa, T. Murakami, K. Takahashi, H. Matsumoto, K. Wakamori, and Y. Arimoto, "Performance evaluation of next generation free-space optical communication system," *IEICE Trans. Electron.*, vol. 90, no. 2, pp. 381–388, Feb. 2007.

[21] S. M. Walsh, S. F. E. Karpathakis, A. S. McCann, B. P. Dix-Matthews, A. M. Frost, D. R. Gozzard, C. T. Gravestock, and S. W. Schediwy, "Demonstration of 100 gbps coherent free-space optical communications at LEO tracking rates," *Sci. Rep.*, vol. 12, no. 1, p. 18345, Oct. 2022.

[22] V. V. Mai and H. Kim, "Airborne free-space optical communications for fronthaul/backhaul networks of 5G and beyond," *IEEE Future Netw. Tech Focus*, vol. 4, no. 1, pp. 1–5, Jul. 2021.

[23] D. of Atmospheric Sci. (DAS) at Univ. Illinois at Urbana-Champaign. (2023). *Diffraction of Light: Light Bending Around an Object*. [Online]. Available: http://ww2010.atmos.uiuc.edu/

[24] (2023). *Why Does the James Webb Telescope Show Stars With 8 Points?*. [Online]. Available: https://www.bbc.com/portuguese/geral-62163554

[25] (2023). *Diffraction Patterns Behind Different Apertures*. [Online]. Available: https://www.lighttrans.com/use-cases/application/diffraction-patterns-behind-different-apertures.html

[26] (2023). *Image Filtering—MorphologyEx()*. [Online]. Available: https://docs.opencv.org/4.x/d4/d86/group_imgproc_filter.html

[27] (2023). *Image Filtering—MorphTypes*. [Online]. Available: https://docs.opencv.org/4.x/d4/d86/group_imgproc_filter.html

[28] A. C. Campos. (2023). *Visible Beam Characterization*. [Online]. Available: https://github.com/AndreCCampos25/Ellipse_Redpixels_Code.git

[29] R. Kwiatkowski. (2023). *Gradient Descent Algorithm? A Deep Dive*. [Online]. Available: https://towardsdatascience.com/gradient-descent-algorithm-a-deep-dive-cf04e8115f21

[30] M. M. Freitas, M. A. Fernandes, P. P. Monteiro, F. P. Guiomar, and G. M. Fernandes, "Requirements and solutions for robust beam alignment in fiber-coupled free-space optical systems," *Photonics*, vol. 10, no. 4, p. 394, Apr. 2023.

[31] M. A. Fernandes, P. P. Monteiro, and F. P. Guiomar, "Single-wavelength terabit FSO channel for datacenter interconnects enabled by adaptive PCS," in *Proc. Opt. Fiber Commun. Conf. Exhibition (OFC)*, Jun. 2021, pp. 1–3.

[32] H. Tataria, M. Shafi, A. F. Molisch, M. Dohler, H. Sjöland, and F. Tufvesson, "6G wireless systems: Vision, requirements, challenges, insights, and opportunities," *Proc. IEEE*, vol. 109, no. 7, pp. 1166–1199, Jul. 2021.

[33] A. Jahid, M. H. Alsharif, and T. J. Hall, "A contemporary survey on free space optical communication: Potentials, technical challenges, recent advances and research direction," *J. Netw. Comput. Appl.*, vol. 200, Apr. 2022, Art. no. 103311.

[34] A. Fayad, T. Cinkler, and J. Rak, "5G/6G optical fronthaul modeling: Cost and energy consumption assessment," *J. Opt. Commun. Netw.*, vol. 15, no. 9, pp. D33–D46, 2023.

[35] M. Alzenad, M. Z. Shakir, H. Yanikomeroglu, and M.-S. Alouini, "FSO-based vertical backhaul/fronthaul framework for 5G+ wireless networks," *IEEE Commun. Mag.*, vol. 56, no. 1, pp. 218–224, Jan. 2018.

[36] A. A. Sabri, S. M. Hameed, and W. A. H. Hadi, "Last mile access-based FSO and VLC systems," *Appl. Opt.*, vol. 62, no. 31, p. 8402, 2023.

[37] N. J. Nzekwu, M. A. Fernandes, G. M. Fernandes, P. P. Monteiro, and F. P. Guiomar, "A comprehensive review of UAV-assisted FSO relay systems," *Photonics*, vol. 11, no. 3, p. 274, Mar. 2024.

[38] Z. Qadir, K. N. Le, N. Saeed, and H. S. Munawar, "Towards 6G Internet of Things: Recent advances, use cases, and open challenges," *ICT Exp.*, vol. 9, no. 3, pp. 296–312, 2023.
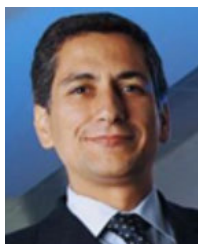
ANDRÉ C. CAMPOS (Member, IEEE) received the M.Sc. degree in electronics and telecommunications engineering from the University of Aveiro, in 2023. His thesis was titled "Computer Vision for Automatic Optical Beam Steering in Free-Space Optics Systems" and the work described in it was used within the scope of this manuscript. His research interests include free space optics (FSO) communications and computer vision.

PETIA GEORGIEVA (Senior Member, IEEE) is currently a Professor in machine learning with the Department of Electronics Telecommunications and Informatics, University of Aveiro, Portugal, a Senior Researcher with the Institute of Electronics and Informatics Engineering of Aveiro (IEETA), Portugal, and a Collaborator Member of the Institute of Telecommunications, Aveiro. Previously, she had academic positions with the University of Porto (2001–2003) and research visiting positions with Rowan University, USA, Carnegie Mellon University, USA, University of Lancaster, U.K., and Bulgarian Academy of Sciences, Bulgaria. Her research interests include machine learning, deep learning, and data mining. Her work involves the implementation of AI techniques in diverse scenarios and use cases, such as medical imaging, optical and wireless communications, robotics, smart homes, and brain–computer interfaces. She has published more than 150 publications in international journals, books, book chapters, and conference proceedings. She is a Senior Member of International Neural Network Society (INNS).
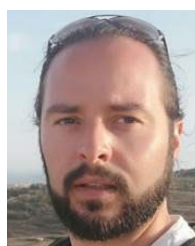
MARCO A. FERNANDES (Member, IEEE) received the M.Sc. degree in electronics and telecommunications engineering from the University of Aveiro, in 2019, and the joint Ph.D. degree from the University of Aveiro, University of Porto, and University of Minho, through the MAP-Tele Doctorate Program, in 2023. During the M.Sc. degree, he worked with analog-radio over fiber applied to 5G communications. His Ph.D. was focused on high-capacity, reliable free space optics (FSO) communications exploiting coherent optics, advanced modulation techniques, and machine-learning-based channel estimation. Currently, he is a Postdoctoral Researcher participating in multiple research projects, mainly involving high capacity FSO transmission for terrestrial and satellite applications. He has already authored or coauthored more than 40 scientific publications in leading international journals and conferences. He is a member of Optica. In 2021, he was a Finalist with the OFC2021 Corning Student Award, and in 2023, he was a Runner-Up at the ECOC Best Student Paper Award.

GIL M. FERNANDES (Member, IEEE) received the degree in physics and in applied mathematics from the Faculdade de Ciências, University of Porto, in January 2008, and the M.Sc. degree in physics engineering and the Ph.D. degree in electrical engineering from the University of Aveiro, Portugal, in December 2010 and December 2018, respectively. He has been a Lecturer with the Physics Department, University of Aveiro, since 2019, where he teaches courses related to optics and physics. Currently, he is a Researcher with the Instituto de Telecomunicações, Aveiro, where he has contributed as a member of the principal team in more than ten research and development projects and has coauthored more than 40 scientific publications in leading international journals and conferences. His primary research interests include high-capacity fiber-optic and optical wireless communication systems, digital signal processing, and optical signal processing.

PAULO P. MONTEIRO (Senior Member, IEEE) is currently an Associate Professor with the University of Aveiro and a Senior Researcher with the Instituto de Telecomunicações, where he is also a Research Coordinator in optical communication systems (https://www.it.pt/Groups/Index/59) with the Instituto de Telecomunicações. His main research interests include optical communications, fixed mobile convergence, and reflectometry systems. Successfully tutored over 15 Ph.D.'s, 24 master's, and participated in more than 26 research projects. He has authored/coauthored more than 18 patent applications, over 157 articles in journals, and 290 conference contributions. He is a Coordinator of the research infrastructure.

FERNANDO P. GUIOMAR (Senior Member, IEEE) received the M.Sc. and Ph.D. degrees in electronics and telecommunications engineering from the University of Aveiro, Portugal, in 2009 and 2015, respectively. In 2015, he has received a Marie Skodowska-Curie Individual Fellowship, jointly hosted by the Politecnico di Torino, Italy, and CISCO Optical GmbH, Nuremberg. In 2016, he received the Photonics21 Student Innovation Award, distinguishing industrial-oriented research with high impact in Europe. Since 2017, he has been a Senior Researcher with the Instituto de Telecomunicações Aveiro. He has authored or coauthored more than 150 scientific publications in leading international journals and conferences. His main research interests include fiber-based and free-space optical communication systems, including the development of digital signal processing algorithms, advanced modulation and coding, constellation shaping, and nonlinear modeling and mitigation. He is a member of OSA.

• • •